A General Maximum Energy Efficiency Tracking Scheme for Domino Wireless Power Transfer Systems With Quasi-Load-Independent Outputs

Kaiyuan Wang, *Student Member, IEEE*, Junming Zeng, *Student Member, IEEE*, Yun Yang, *Senior Member, IEEE*, and Shu Yuen Ron Hui, *Fellow, IEEE*

***Abstract*—This article presents a double-layer pulsewidth pulse-frequency based optimal control (PWPFC) in achieving maximum energy efficiency tracking (MEET) and quasi-load-independent (QLI) constant current (CC) and constant voltage (CV) outputs for domino wireless power transfer (WPT) systems with full considerations of equivalent series resistances. The proposed hierarchical control, which can be implemented using inexpensive digital controllers, is applied to the primary-side inverters based on the measured output current, output voltage, and phase angle of the receiver current via infrared communication. The upper layer (i.e., stage-I) of the PWPFC is a reference selection algorithm to provide references of operating frequencies and duty ratios for the tracking algorithm of the lower layer (i.e., stage-II). To ensure accurate tracking, a hill-climbing method is adopted to regulate the operating frequency of practical domino WPT systems with parasitic components and disturbance. Experimental results have verified the effectiveness of the proposed PWPFC in regulating domino WPT systems with MEET and QLI CC and CV outputs under various loads, compensation networks, and initial frequency conditions.**

***Index Terms*—Domino wireless power transfer (WPT), maximum energy efficiency transfer, pulse-width pulse-frequency-based optimal control (PWPFC), quasi-load-independent (QLI) outputs.**

I. Introduction

DOMINO wireless power transfer (WPT) refers to a mid-range or long-range WPT system with relay coils between the transmitter and receiver resonators [1]. Relay coils are generally compensated by capacitors to form medium resonators to enhance the power transfer efficiency [2], [3], [4], [5]. By far, fundamentals of domino WPT systems have been extensively investigated [6], [7], [8], [9], [10], [11], [12], [13]. General analyses of domino WPT systems without considering the cross-coupling effects are reported in [6] and [7]. Optimal load conditions in achieving maximum efficiencies at the resonant frequencies are derived for different domino configurations. In [8], the basic characteristics of domino WPT systems with noncoaxial resonators are primarily explained. Optimal operating frequencies are revealed to be slightly different from the resonant frequencies due to multipower path effects of noncoaxial resonators. The maximum efficiencies of WPT systems can be achieved by regulating the operating frequencies of the driving circuits. The domino WPT systems with series compensation schemes are simplified as two-stage WPT systems for constant current (CC) and constant voltage (CV) control [9], [10]. In [9], the operating frequency is selected to guarantee both the system stability and zero phase angle. Similar key frequencies are obtained via a quadratic eigenvalue model in [11]. Apart from series compensated domino WPT systems, other compensation networks (i.e., *LCC-LCC*) are also studied in achieving CC and CV outputs [12], [13]. Smooth transitions from the CC mode to the CV mode are implemented by specific circuit parameter designs. Besides, domino WPT systems are modified to have multiple outputs by integrating loads to the medium resonators [14], [15], [16], [17], [18], [19]. In [14] and [15], CC outputs are implemented. In [16] and [17], CV outputs can be achieved. Hybrid CC and CV outputs are realized in [18] and [19]. To eliminate the cross couplings between the nonadjacent coils, bipolar coupler configurations are adopted for the medium resonators in all those systems.

One promising application of the domino WPT system is to place the system in high voltage insulators to harvest energy from the transmission lines to the sensors on the power towers [20], [21], [22], [23], [24], [25], [26], since the inductive-type WPT operating at kilohertz frequency levels will not affect electric fields and voltage distribution of the insulators [27]. To reduce the weight and size of the resonators, printed circuit board (PCB) based resonators are designed for the insulators [21]. On this basis, more comprehensive analysis, modeling, and optimization of the PCB resonators are conducted in [22]. In [23], the system transfer efficiency is improved by the optimization of spacing between the domino coils. To achieve fixed-frequency CC and CV outputs, a configurable compensation network for

Manuscript received 4 July 2023; revised 10 September 2023 and 10 October 2023; accepted 14 October 2023. Date of publication 17 October 2023; date of current version 6 December 2023. This work was supported in part by NTU Start Up under Grant 03INS001563C140 and in part by the Ministry of Education (MoE) Academic Research Fund (AcRF) Tier-1 under Grant RG116/21. Recommended for publication by Associate Editor A. Kuperman. *(Corresponding author: Yun Yang.)*

Kaiyuan Wang, Junming Zeng, and Yun Yang are with the Nanyang Technological University, Singapore 639798 (e-mail: kaiyuan002@e.ntu.edu.sg; zeng0141@e.ntu.edu.sg; yun.yang@ntu.edu.sg).

Shu Yuen Ron Hui is with the Imperial College London, SW7 2BX London, U.K., and also with the University of Hong Kong, Hong Kong (e-mail: ronhui@eee.hku.hk).

Color versions of one or more figures in this article are available at https://doi.org/10.1109/TPEL.2023.3325307.

Digital Object Identifier 10.1109/TPEL.2023.3325307

the receiver (i.e., *LCC* compensation for CC output while series compensation for CV output) is implemented in [24]. In [25], a distributed series compensation method is employed for a double-layer domino cylindrical solenoid coupler within post insulators. As a result, the resistances attributed to the stray capacitances can be diminished. The domino WPT system has also been applied for insulating pillars [26].

This article focuses on addressing two fundamental issues of domino WPT systems that have never been investigated before. The first issue is the effects of equivalent series resistances (ESRs) of the resonators on the outputs. For ideal domino WPT systems, load-independent CC and CV outputs can be achieved at some operating frequencies. However, when the ESRs of the resonators are considered, the load-independent characteristics are lost. Instead, quasi-load independent (QLI) outputs can be achieved by well-designed controllers. This article provides comprehensive analyses and systematic design methods for domino WPT systems with QLI CC and CV outputs. The second issue is the number of frequencies for load-independent or QLI CC and CV outputs are multiple. Thus, to proper select of the operating frequencies is an open problem that has not been fully resolved by the pioneers. This article aims to bridge the research gap by developing a new control algorithm to find out and then lock the optimal frequencies for maximum energy efficiency tracking (MEET).

The proposed control algorithm is a double-layer pulse-width pulse-frequency based optimal control (PWPFC). The upper layer (i.e., stage-I) is a reference selection algorithm that outputs the references of both the operating frequency and the duty ratio of the transmitter driving circuit, while the lower layer (i.e., stage-II) is a tracking algorithm to track the derived references. In stage I, the frequency reference is selected among the eligible operating frequencies (that satisfy the requirements of voltage gains and output deviations) in achieving MEET. The duty ratio reference is determined based on the conventional self-oscillating algorithm in [28] to feed back the phase angle of the receiver current. According to the analyses in this article, the duty ratio reference is 0.25 for CC outputs, while it is 0 or 0.5 for CV outputs. In stage 2, the duty ratio reference is directly adopted as the duty ratio of the switching signal, while the frequency reference is used as the initial operating frequency. The optimal operating frequency for MEET is searched out by a hill-climbing method for accurate tracking, since the calculated frequency reference may not be accurate due to parasitic components and disturbance.

Comprehensive comparisons among the proposed control strategy and the existing control strategies are given in Table I. Apparently, the proposed PWPFC has two merits that could attract attentions from industry. The first merit is that both high efficiency and accurate output regulations can be achieved for a practical domino WPT systems with nonignorable ESRs. The second merit is the simple algorithms which can easily implemented using inexpensive digital controllers. The main contributions of the article include the following: a comprehensive control framework for general domino WPT systems in achieving QLI CC and CV outputs with maximum efficiencies (automatic operating frequency locking at fixed values for MEET has not been investigated before); a robust PWPFC being designed for practical domino WPT systems with the considerations of ESRs and variable load conditions; and a general control strategy for domino WPT systems with other compensation networks rather than the series-series (SS) compensation only.

TABLE I
COMPARISONS AMONG THE PROPOSED AND EXISTING METHODS

Reference	Output Type	Compensation Type	Additional Circuit	Consider ESRs	MEET
Dong et al. [9]	CC	SS	No	No	No
Hou et al. [11]	CC&CV	SS	No	Yes	No
Hou et al. [12]	CC&CV	LCC-LCC	No	Yes	No
Wang et al. [13]	CC&CV	LCC-S	Yes	No	No
Yan et al. [24]	CC&CV	S-LCC	Yes	Yes	No
Gu et al. [26]	CV	CLC-CLC	No	No	No
This article	CC&CV	Any	No	Yes	Yes

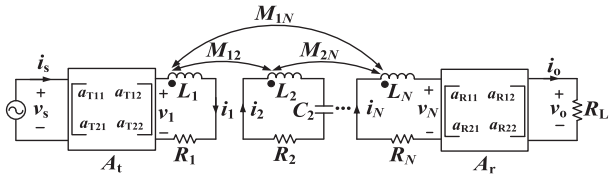

Fig. 1. Equivalent circuit diagram of a typical domino WPT system.

The rest of this article is organized as follows. In Section II, the QLI CC and CV characteristics of typical domino WPT systems, including the effects of ESRs, are meticulously analyzed. In Section III, the proposed double-layer PWPFC based on the analyses in Section II is explained with technical details and some simulation results. In Section IV, experimental verifications of the proposed control for domino WPT systems under various conditions are presented. Finally, Section V concludes this article work.

II. SYSTEM ANALYSIS WITH CONSIDERATIONS OF ESRS

The equivalent circuit of a typical domino WPT system, which consists of a high-frequency power supply v_s, a transmitter coil L_1 and its compensation network $\boldsymbol{A_t}$, a receiver coil L_N and its compensation network $\boldsymbol{A_r}$, multiple relay resonators, and a resistive load R_L, is depicted as shown in Fig. 1. Here, i_s and i_o are the transmitter and receiver currents. v_o is the output voltage. $\boldsymbol{A_t}$ and $\boldsymbol{A_r}$ represent the matrices of the compensation networks (i.e., series, parallel, *LC*, and *LCC*). L_i ($i = 2, \ldots, N$-1) denotes the self-inductances of the ith relay coil. C_i ($i = 2, \ldots, N$-1) is the compensated capacitances for the relay coils. The ESRs of the relay resonators are R_i ($i = 2, \ldots, N$-1). M_{ij} ($i \neq j$) signifies the mutual inductance between the ith and jth coil.

To simplify the analysis without losing generality, the self-inductances of the coils, compensated capacitors of the relay resonators, and the mutual inductances are assumed to be equal. Then, the resonant frequencies of the relay resonators are as follows:

$$\omega_o = \frac{1}{\sqrt{L_i C_i}} \, (i = 2,\ 3, \ldots,\ N-1)\,. \tag{1}$$

By applying the Kirchhoff's laws

$$\begin{cases} \sum_{i=1}^{N-1} j\omega M_{Ni} i_i + Z_r\, i_N = -\left(a_{R11} R_L + a_{R12}\right) i_{\mathrm{o}} \\ i_N = \left(a_{R21} R_L + a_{R22}\right)\, i_{\mathrm{o}} \\ v_1 = Z_t\, i_1 + \sum_{i=2}^{N} j\omega M_{1i} i_i \end{cases} \tag{2}$$

where $Z_t = j\omega L_1 + R_1$ and $Z_{\mathrm{r}} = j\omega L_N + R_N$ are the transmitter and receiver coil impedances, respectively. a_{R11}, a_{R12}, a_{R21}, and a_{R22} are the *ABCD* parameters of the receiver compensation network

Based on (2), a general expression of the domino WPT system can be derived as (3.1) shown at the bottom of this page, where a_{T11}, a_{T12}, a_{T21}, a_{T22} are the *ABCD* parameters of the transmitter compensation network

$$Z_{t1} = \frac{a_{T12}}{a_{T11}} + Z_t \tag{3.2}$$

$$Z_{r1} = \frac{a_{R11} R_L + a_{R12}}{a_{R21} R_L + a_{R22}} + Z_r \tag{3.3}$$

$$Z_i = j\left(\omega L_i - \frac{1}{\omega C_i}\right) + R_i \;\; (i = 2, \ldots,\; N-1)\,. \tag{3.4}$$

Then, the currents of the relay coils (i.e., *I*) can be derived as

$$\boldsymbol{I} = -\boldsymbol{D}^{-1}\left[\boldsymbol{C} i_1 + \boldsymbol{E}\left(a_{R21} R_{\mathrm{L}} + a_{R22}\right) i_{\mathrm{o}}\right] \tag{4}$$

where $\boldsymbol{I} = \begin{bmatrix} i_2 \\ i_3 \\ \vdots \\ i_{N-1} \end{bmatrix}$, $\boldsymbol{C} = \begin{bmatrix} j\omega M_{21} \\ j\omega M_{31} \\ \vdots \\ j\omega M_{N1} \end{bmatrix}$,

$\boldsymbol{D} = \begin{bmatrix} Z_2 & j\omega M_{23} & \cdots & j\omega M_{2(N-1)} \\ j\omega M_{32} & Z_3 & \cdots & j\omega M_{3(N-1)} \\ \vdots & \vdots & \ddots & \vdots \\ j\omega M_{N2} & j\omega M_{N3} & \cdots & j\omega M_{N(N-1)} \end{bmatrix}$, and

$\boldsymbol{E} = \begin{bmatrix} j\omega M_{2N} \\ j\omega M_{3N} \\ \vdots \\ Z_{\mathrm{r1}} \end{bmatrix}$.

By substituting (4) into the first and last rows of (3.1)

$$\begin{bmatrix} \frac{v_s}{a_{T11}} \\ 0 \end{bmatrix} = \begin{bmatrix} Z_{t1} - \alpha & \left(j\omega M_{1N} - \gamma\right)\left(a_{R21} R_L + a_{R22}\right) \\ j\omega M_{N1} - \beta & \left(Z_{r1} - \delta\right)\left(a_{R21} R_L + a_{R22}\right) \end{bmatrix} \times \begin{bmatrix} i_1 \\ i_{\mathrm{o}} \end{bmatrix} \tag{5}$$

where $\alpha = \boldsymbol{A}\boldsymbol{D}^{-1}\boldsymbol{C}$, $\beta = \boldsymbol{B}\boldsymbol{D}^{-1}\boldsymbol{C}$, $\gamma = \boldsymbol{A}\boldsymbol{D}^{-1}\boldsymbol{E}$, $\delta = \boldsymbol{B}\boldsymbol{D}^{-1}\boldsymbol{E}$, $\boldsymbol{A} = \begin{bmatrix} j\omega M_{12} & j\omega M_{13} & \cdots & j\omega M_{1(N-1)} \end{bmatrix}$, $\boldsymbol{B} = \begin{bmatrix} j\omega M_{N2} & j\omega M_{N3} & \cdots & j\omega M_{N(N-1)} \end{bmatrix}$.

To analyze the output characteristics of the domino WPT system, γ and δ need to be further simplified as

$$\gamma = \left(\boldsymbol{A}\boldsymbol{D}^{-1}\right)\boldsymbol{E} = \sum_{i=1}^{N-2} a_i c_i + a_{(N-1)} Z_{r1} \tag{6.1}$$

$$\delta = \left(\boldsymbol{B}\boldsymbol{D}^{-1}\right)\boldsymbol{E} = \sum_{i=1}^{N-2} b_i c_i + b_{(N-1)} Z_{r1} \tag{6.2}$$

where $\boldsymbol{A}\boldsymbol{D}^{-1}$, $\boldsymbol{B}\boldsymbol{D}^{-1}$, and $\boldsymbol{E}$ are expressed as

$$\boldsymbol{A}\boldsymbol{D}^{-1} = \begin{bmatrix} a_1 & a_2 & \cdots & a_{N-1} \end{bmatrix} \tag{6.3}$$

$$\boldsymbol{B}\boldsymbol{D}^{-1} = \begin{bmatrix} b_1 & b_2 & \cdots & b_{N-1} \end{bmatrix} \tag{6.4}$$

$$\boldsymbol{E} = \begin{bmatrix} c_1 & c_2 & \cdots & c_{N-1} & Z_{\mathrm{r1}} \end{bmatrix}^T. \tag{6.5}$$

By substituting (6) into (5)

$$\begin{bmatrix} v_s \\ 0 \end{bmatrix} = \begin{bmatrix} a_{T12} + a_{T11}\left(Z_t - \alpha\right) & a_{T11}\left(F_1 + F_2 R_L\right) \\ j\omega M_{N1} - \beta & G_1 + G_2 R_L \end{bmatrix} \begin{bmatrix} i_1 \\ i_{\mathrm{o}} \end{bmatrix} \tag{7.1}$$

where

$$F_1 = a_{R22}\left(j\omega M_{1N} - \sum_{i=1}^{N-2} a_i c_i\right) - a_{N-1}\left(a_{R22} Z_r + a_{R12}\right) \tag{7.2}$$

$$F_2 = a_{R21}\left(j\omega M_{1N} - \sum_{i=1}^{N-2} a_i c_i\right) - a_{N-1}\left(a_{R21} Z_r + a_{R11}\right) \tag{7.3}$$

$$G_1 = \left(1 - b_{N-1}\right)\left(a_{R22} Z_r + a_{R12}\right) - a_{R22} \sum_{i=1}^{N-2} b_i c_i \tag{7.4}$$

$$G_2 = \left(1 - b_{N-1}\right)\left(a_{R21} Z_r + a_{R11}\right) - a_{R21} \sum_{i=1}^{N-2} b_i c_i. \tag{7.5}$$

Based on (7), the relationships between the system input voltage (i.e., v_s) and output current and voltage (i.e., i_o and v_o) can be derived as

$$v_s = \left[f_v(\omega) + f_c(\omega) R_L\right]\, i_o \tag{8.1}$$

$$v_s = \left[\frac{f_v(\omega)}{R_L} + f_c(\omega)\right]\, v_o \tag{8.2}$$

where $f_v(\omega)$ and $f_c(\omega)$ are the functions of ω, which can be expressed as

$$f_v(\omega) = \frac{\left[a_{T12} + a_{T11}\left(Z_t - \alpha\right)\right] G_1}{j\omega M_{N1} - \beta} - a_{T11} F_1 \tag{8.3}$$

$$\begin{bmatrix} \frac{v_s}{a_{T11}} \\ 0 \\ 0 \\ \vdots \\ 0 \end{bmatrix} = \begin{bmatrix} Z_{t1} & j\omega M_{12} & j\omega M_{13} & \cdots & j\omega M_{1N} \\ j\omega M_{21} & Z_2 & j\omega M_{23} & \cdots & j\omega M_{2N} \\ j\omega M_{31} & j\omega M_{32} & Z_3 & \cdots & j\omega M_{3N} \\ \vdots & \vdots & \vdots & \ddots & \vdots \\ j\omega M_{N1} & j\omega M_{N2} & j\omega M_{N3} & \cdots & Z_{\mathrm{r1}} \end{bmatrix} \begin{bmatrix} i_1 \\ i_2 \\ i_3 \\ \vdots \\ \left(a_{R21} R_{\mathrm{L}} + a_{R22}\right) i_{\mathrm{o}} \end{bmatrix}. \tag{3.1}$$

TABLE II
PARAMETERS OF AN IDEAL FOUR-COIL DOMINO WPT SYSTEM

Parameters	Symbol	Value
Self-inductance of the coils (i=1, 2, 3, 4)	L_i	49.5 μH
Compensated capacitances (i=1, 2, 3, 4)	C_i	12.9 nF
Resonant frequency of the system	f_o	200 kHz
Mutual inductances between the neighboring coils	M_{12}, M_{23}, M_{34}	9.737 μH
Mutual inductances between the alternate coils	M_{13}, M_{24}	3.623 μH
Mutual inductance between the transmitter and receiver coils	M_{14}	1.737 μH

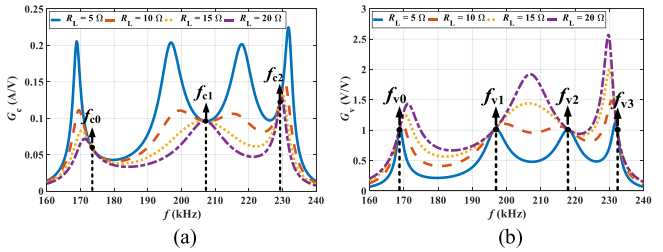

Fig. 2. Characteristics of (a) G_c and (b) G_v of the ideal (no ESRs) four-coil domino WPT system with different load conditions.

$$f_c(\omega) = \frac{[a_{T12} + a_{T11}(Z_t - \alpha)]\, G_2}{j\omega M_{N1} - \beta} - a_{T11} F_2. \tag{8.4}$$

It is worth noting that $f_v(\omega)$ and $f_c(\omega)$ are independent of the load conditions but are coupled with the operating frequency and other system parameters. The expressions (8.3) and (8.4) are formulated to simplify the expressions of (8.1) and (8.2), which establish the relationships between the input voltage and output voltage and current of the resonators. According to (8.1), the load-independent CC output of the domino WPT system can be achieved by controlling the operating frequency ω to satisfy $f_c(\omega) = 0$. The corresponding transconductance of the system is

$$G_c = \frac{I_o}{V_s} = \left| \frac{1}{f_v(\omega)} \right| \quad f_v(\omega) \neq 0. \tag{9}$$

According to (8.2), the load-independent CV output of the domino WPT system can be implemented by regulating the operating frequency ω to satisfy $f_v(\omega) = 0$. The corresponding voltage gain of the system is

$$G_v = \frac{V_o}{V_s} = \left| \frac{1}{f_c(\omega)} \right| \quad f_c(\omega) \neq 0 \tag{10}$$

where V_o is the RMS value of v_o. The derived G_c and G_v of an ideal domino WPT system based on (9) and (10) are identical to the ones in [9]. More details of load-independent CC and CV operations for domino WPT systems with small ESRs can be found in [29].

It is worth noting that the solutions for $f_c(\omega) = 0$ or $f_v(\omega) = 0$ are not unique, which means more than one operating frequency can achieve load-independent CC or CV output for an ideal domino WPT system with no ESRs. The characteristics of G_c and G_v of an ideal four-coil SS-compensated domino WPT system with the parameters in Table II, are plotted as shown in Fig. 2. The operating frequency of the system ranges from 160 to 240 kHz, which is compliant with the most existing

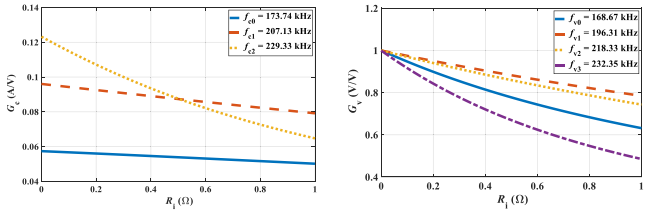

Fig. 3. Characteristics of (a) G_c and (b) G_v of the nonideal domino WPT system with $R_L = 10\ \Omega$ and different ESRs.

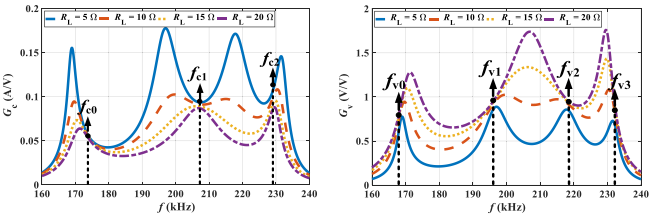

Fig. 4. Characteristics of (a) G_c and (b) G_v of the nonideal domino WPT system with ESR $= 0.3\ \Omega$ and different load conditions.

domino WPT systems operating at kilohertz levels [9], [13], [15], [18], [24]. Apparently, the WPT system has three critical frequencies (i.e., $f_{c0} = 173.74$ kHz, $f_{c1} = 207.13$ kHz, and $f_{c2} = 229.33$ kHz) within the spectrum from 160 to 240 kHz ($\pm$20% of the resonant frequency) to achieve load-independent CC outputs and four critical frequencies (i.e., $f_{v0} = 168.67$ kHz, $f_{v1} = 196.31$ kHz, $f_{v2} = 218.33$ kHz, and $f_{v3} = 232.35$ kHz) to achieve load-independent CV outputs. The load resistance R_L is changed from 5 to 20 Ω. For load-independent CC outputs, the transconductances of the three critical frequencies are different (i.e., $G_c(f_{c0}) = 0.0574$, $G_c(f_{c1}) = 0.0960$, and $G_c(f_{c2}) = 0.123$). However, the voltage gains of the four critical frequencies for load-independent CV outputs are unity. Proofs of unity voltage gains for the ideal four-coil domino WPT system are provided in Appendix A.

For nonideal domino WPT systems with a fixed $R_L = 10\ \Omega$, both G_c and G_v will decrease as the ESRs (i.e., R_i) are increased. The plotted simulation curves are shown in Fig. 3. The coupled coils with higher quality factors can result in higher G_c and G_v. To facilitate the analyses within the investigated frequency spectrum, the variation of ac ESRs caused by skin and proximity effects are neglected. Without losing the generality of the proposed control strategy, the ESRs are considered to be constant in this article. For fixed ESRs (e.g., $R_i = 0.3\ \Omega$), as the load resistance R_L increases, G_c will decrease while G_v will increase. The curves of G_c and G_v for the nonideal four-coil domino WPT system with $R_i = 0.3\ \Omega$ are plotted in Fig. 4. Compared to the results in Fig. 2, small deviations of G_c and G_v among different load conditions exist at the critical frequencies. QLI outputs are realized instead of ideal load-independent outputs. To quantify the degrees of deviations, the relative errors between practical G_c or G_v (with considering ESRs) and ideal G_c or G_v (without

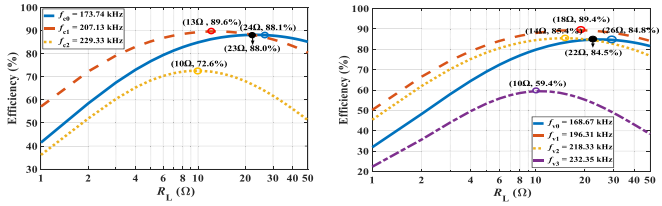

Fig. 5. Efficiencies of the domino resonators at critical frequencies with ESR = 0.3 Ω and different load conditions for QLI (a) CC outputs and (b) CV outputs.

considering ESRs) are calculated using

$$\sigma_c = \left| \frac{G_c - G_{c\_ideal}}{G_{c\_ideal}} \right| \times 100\% \tag{11.1}$$

$$\sigma_v = \left| \frac{G_v - G_{v\_ideal}}{G_{v\_ideal}} \right| \times 100\%. \tag{11.2}$$

Both σ_c and σ_v are important indexes to indicate the qualities of load-independent output regulations. The critical frequency with smaller σ_c or σ_v means better output regulations. In this article, only the critical frequencies with tolerable σ_c or σ_v (i.e., $\sigma_c \le \sigma_{c\max}$ or $\sigma_v \le \sigma_{v\max}$) are chosen as optional frequencies for further selections.

Since the GaN-based power switches are used for the primary-side driving circuit, the inverter loss is negligible as compared to the conduction loss of the coupled resonators. Hence, only the power transfer efficiencies of the resonators need to be simulated and analyzed based on

$$\eta = \frac{I_o^2 R_L}{I_o^2 R_L + \sum_{i=1}^{N} I_i^2 R_i} \tag{12}$$

where I_i is the RMS value of i_i. The efficiencies of the resonators at the critical frequencies (i.e., $f_{c0}, f_{c1}, f_{c2}, f_{v0}, f_{v1}, f_{v2}$, and f_{v3}) with $R_i = 0.3\,\Omega$ and different load conditions are plotted in Fig. 5. For load-independent CC outputs, the efficiencies at f_{c0} and f_{c1} are always greater than f_{c2}. When $R_L < 23\ \Omega$, the efficiency at f_{c1} is greater than that at f_{c0}. On the contrary ($R_L > 23\ \Omega$), the efficiency at f_{c1} is less than that at f_{c0}. when $R_L = 23\ \Omega$, the efficiencies at f_{c0} and f_{c1} are equal. For load-independent CV outputs, the efficiencies at f_{v1} are always greater than those at f_{v0}, f_{v2}, and f_{v3}. When $R_L < 22\ \Omega$, the efficiency at f_{v2} is greater than that at f_{v0}. On the contrary ($R_L > 22\ \Omega$), the efficiency at f_{v2} is less than that at f_{v0}. When $R_L = 22\ \Omega$, the efficiencies at f_{v0} and f_{v2} are equal. This article aims to achieve acceptable output regulations with limited load effects and optimal efficiencies simultaneously. Thus, the efficiencies of the resonators with selected critical frequencies with tolerable σ_c or σ_v are compared. The one with optimal efficiency is chosen as the operating frequency of the system.

III. Proposed Control Strategy

A. Basic Control Algorithms

The control block diagram of the proposed double-layer PWPFC is depicted in Fig. 6. The reference selection algorithm in

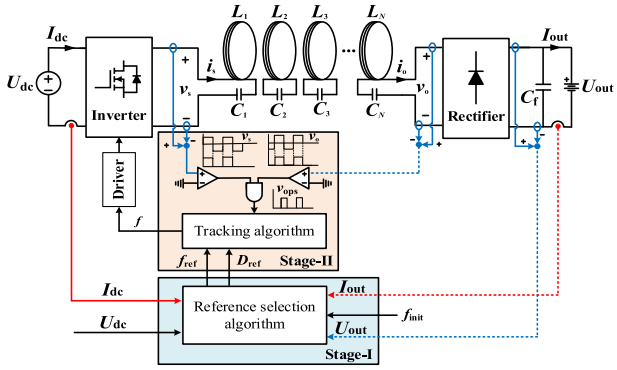

Fig. 6. Control block diagram of the proposed double-layer PWPFC.

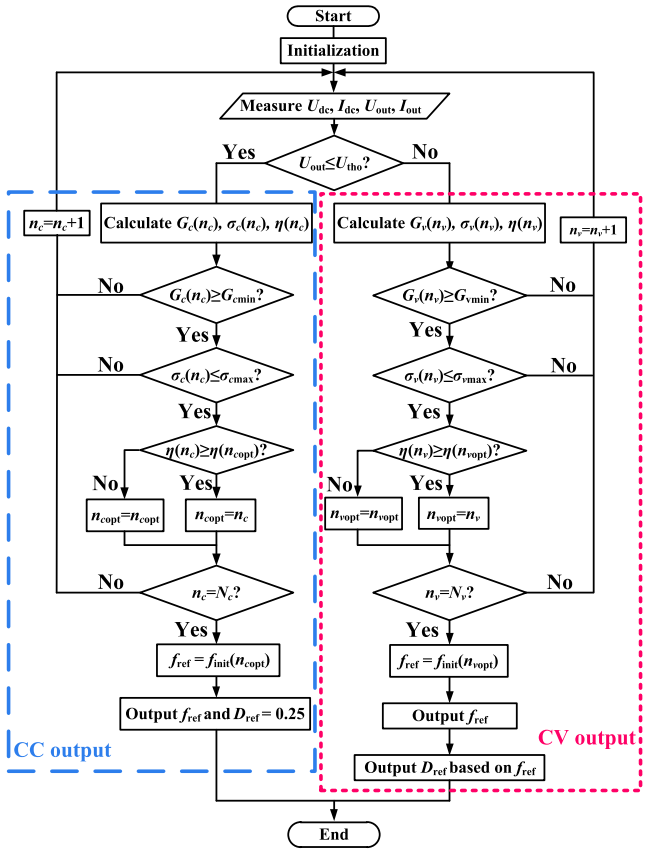

Fig. 7. Flowchart of the reference selection algorithm in stage-I.

the Stage-I is to output the references of frequency (i.e., $f_{\rm ref}$) and duty ratio (i.e., $D_{\rm ref}$) for the tracking algorithm in the stage-II. The inputs of the reference selection algorithm include $I_{\rm out}$ and $U_{\rm out}$ on the receiver side, $U_{\rm dc}$ and $I_{\rm dc}$ on the transmitter side, and the initial operating frequency $f_{\rm init}$ which can be calculated based on (8.3) and (8.4).

The flowchart of the reference selection algorithm is plotted in Fig. 7. N_c and N_v indicate the numbers of QLI CC and CV output points, respectively. For instance, $N_c = 3$ and $N_v = 4$ for the system in Fig. 4. $n_{\rm copt}$ and $n_{\rm vopt}$ indicate the optimal counting number of the operating frequency that results in the

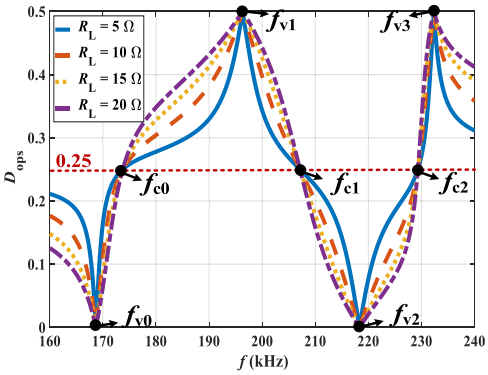

Fig. 8. Duty ratio curves of the domino WPT system with different load conditions.

maximum efficiency. For example, $n_{\mathrm{copt}} = 2$ for the system in Fig. 5(a), since the maximum efficiency is 89.6%. $n_{v\mathrm{opt}} = 2$ for the system in Fig. 5(b), since the maximum efficiency is 89.4%. The initial values of n_c, n_v, n_{copt}, and $n_{v\mathrm{opt}}$ are set to be 1.

The charging mode of the system is selected based on the comparisons between U_{out} and the threshold voltage U_{tho}. If $U_{\mathrm{out}} \leq U_{\mathrm{tho}}$, the CC mode is selected. Otherwise, the CV mode is chosen. In the CC mode, the transconductance $G_c(n_c)$ is calculated based on (9). In the CV mode, the voltage gain $G_v(n_v)$ is calculated based on (10). The first criterion of the reference selection algorithm is to ensure the controllability, such that $G_c(n_c)$ or $G_v(n_v)$ must be greater than the corresponding minimum limit $G_{c\min}$ or $G_{v\min}$. If the first criterion is met, the relative error $\sigma_c(n_c)$ or $\sigma_v(n_v)$ will be calculated based on (11.1) or (11.2) for the second criterion of ensuring the steady-state performance. If $\sigma_c(n_c)$ or $\sigma_v(n_v)$ is less than the maximum limit $\sigma_{c\max}$ or $\sigma_{v\max}$, the overall system efficiency will be calculated based on

$$\eta = \frac{U_{\mathrm{out}} I_{\mathrm{out}}}{U_{\mathrm{dc}} I_{\mathrm{dc}}}. \tag{13}$$

The efficiency $\eta(n_c)$ or $\eta(n_v)$ is compared to $\eta(n_{\mathrm{copt}})$ or $\eta(n_{v\mathrm{opt}})$. If $\eta(n_c)$ or $\eta(n_v)$ is equal or greater than $\eta(n_{\mathrm{copt}})$ or $\eta(n_{v\mathrm{opt}})$, the optimal counting parameter n_{copt} or $n_{v\mathrm{opt}}$ is updated by n_c or n_v. Conversely, n_{copt} or $n_{v\mathrm{opt}}$ remains unchanged. Obviously, the optimal efficiency can be searched out via several iterations until the counting parameter n_c reaching N_c. The optimal frequency will be set as the reference for the tracking algorithm in stage II. For the duty ratio reference D_{ref}, the value is fixed at 0.25 for the CC mode and 0 or 0.5 for the CV mode regardless of ESRs. If the voltage gain G_v is positive, D_{ref} is 0.5. Otherwise, D_{ref} is 0. The proofs are provided in Appendix B. The load-independent duty ratios of the domino WPT system with the parameters given in Table II can be observed from the duty ratio curves in Fig. 8. For the critical frequencies of CC outputs, the duty ratio is 0.25. For the critical frequencies of CV outputs, the duty ratio is either 0 or 0.5.

The stage-II comprises a simple phase detection circuit and a tracking algorithm, which outputs the operating frequency for the transmitter inverter. The phase detection circuit is used to generate the pulse signal of the phase difference between v_{s} and i_{o}. The duty ratio and frequency of the pulse signal are D_{ops} and f_{ops}, respectively. The flowchart of the tracking algorithm is shown in Fig. 9. Initially, the measured D_{ops} at the sampling time k is compared to D_{ref}. If $D_{\mathrm{ops}}(k) = D_{\mathrm{ref}}$ and $f_{\mathrm{ops}} = f_{\mathrm{ref}}(k-1)$, the algorithm terminates. If $D_{\mathrm{ops}}(k) \neq D_{\mathrm{ref}}$, D_{ref} is tracked.

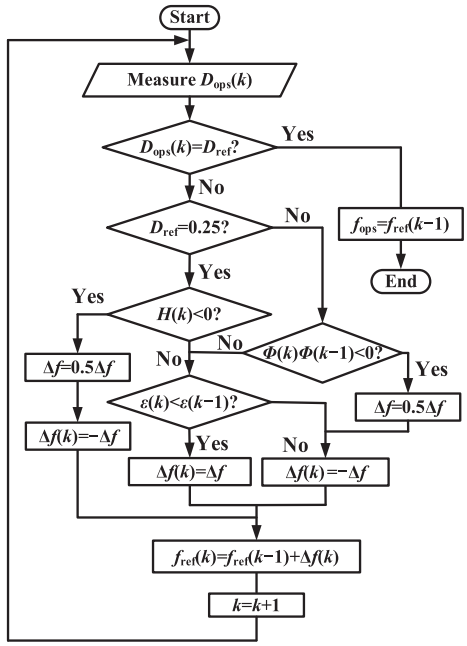

Fig. 9. Flowchart of the tracking algorithm in stage-II.

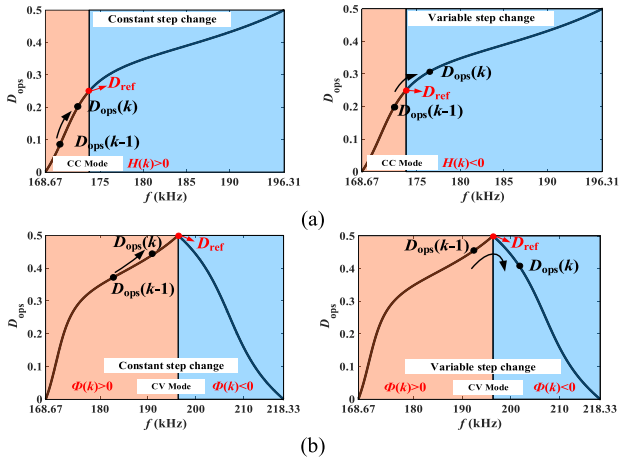

Fig. 10. Searching trajectories of the tracking algorithm for the system in the (a) CC mode and (b) CV mode.

In the CC mode (i.e., $D_{\mathrm{ref}} = 0.25$), the tracking direction is determined by the following intermediate variable:

$$H(k) = [D_{\mathrm{ops}}(k) - D_{\mathrm{ref}}]\,[D_{\mathrm{ops}}(k-1) - D_{\mathrm{ref}}]. \tag{14}$$

The monotonous searching trajectory is shown in Fig. 10(a). $H(k)<0$ indicates the two consecutive points on the searching trajectory are located at different sides of D_{ref}. To ensure the searching accuracy and convergence, the step change of the frequency is halved for $H(k)<0$ and the searching direction is reversed for the next process (i.e., $\Delta f(\mathrm{k}) = -\Delta f/2$). If $H(k)>0$,

the two consecutive searching points are at the same side and the step change of the frequency is constant. Here, the absolute error between $D_{\rm ops}$ and $D_{\rm ref}$ (i.e., $\varepsilon(k) = |D_{\rm ops}(k) - D_{\rm ref}|$) is defined to indicate the searching direction. For instance, $\varepsilon(k) < \varepsilon(k-1)$ means the searching process is getting closer to $D_{\rm ref}$. Thus, the searching direction is correct (i.e., $\Delta f(k) = \Delta f$). On the contrary, $\varepsilon(k) > \varepsilon(k-1)$ means the searching process is moving away from $D_{\rm ref}$. Hence, the searching direction is reversed (i.e., $\Delta f(k) = -\Delta f$).

In the CV mode, the searching trajectory is nonmonotonous, as shown in Fig. 10(b). the tracking direction is determined by the following intermediate variable:

$$\Phi(k) = \frac{D_{\rm ops}(k) - D_{\rm ops}(k-1)}{\Delta f(k-1)} \tag{15}$$

where $\Delta f(k-1)$ is the step change of the operating frequency. $\Phi(k)\Phi(k-1) > 0$ indicates the two consecutive points on the searching trajectory are located at the same side, while $\Phi(k)\Phi(k-1) < 0$ indicates the points at different sides. Similar to the CC mode, the frequency change is halved and the searching direction is reversed for the next process when the two consecutive points are at different sides. For the two consecutive points at the same side, $\varepsilon(k)$ is compared to $\varepsilon(k-1)$. If $\varepsilon(k) < \varepsilon(k-1)$, the searching direction is unchanged with constant frequency steps. Conversely, the searching direction is reversed with constant frequency steps.

The operating frequency of the system is updated for each iteration until $D_{\rm ops}$ reaching $D_{\rm ref}$. The output of the tracking algorithm is the operating frequency. It is worth noting that the regulations of $D_{\rm ops}(k)$ to track $D_{\rm ref}$ is essentially the same as the regulations of v_s is phase with i_o, since the basic idea is to control the operating frequency of the system in achieving $f_c(\omega)$ as a pure real number and $f_v(\omega)$ as a pure imaginary number.

B. Determination of f_{init} for the Reference Selection Algorithm

The basic control algorithm can be directly used for domino WPT systems with small or even negligible ESRs of resonators, since $f_{\rm init}$ can be accurately determined by equalizing (8.3) or (8.4) to zero. For the systems with large ESRs, the properties of $f_c(\omega)$ and $f_v(\omega)$ are complex. The calculated $f_{\rm init}$ based on (8.3) and (8.4) could deviate from the target the value with large discrepancies. Instead, $f_{\rm init}$ can be numerically determined by

$$\Re\{f_v(\omega)\} + \Re\{f_c(\omega)\}\frac{U_{\rm out}}{I_{\rm out}} = 0 \tag{16.1}$$

$$\Im\{f_v(\omega)\} + \Im\{f_c(\omega)\}\frac{U_{\rm out}}{I_{\rm out}} = 0. \tag{16.2}$$

Here, (16.1) is used for determining $f_{\rm init}$ in the CC mode, while (16.2) is for the CV mode. $U_{\rm out}$ and $I_{\rm out}$ are real-time measured outputs.

The load resistances of domino WPT systems will also affect the determination of $f_{\rm init}$. For the domino WPT system with the parameters given in Table II, the differences between $f_{\rm init}$ being calculated based on (8.3) or (8.4) and (16.1) or (16.2) can be plotted, as shown in Fig. 11. Three initial frequencies f_{c0}, f_{c1}, and f_{c2} are calculated for the CC output, while four initial frequencies f_{v0}, f_{v1}, f_{v2}, and f_{v3} are calculated for the CV output. Obviously, in the CC mode, the relative errors between the two calculated results will decrease as the load resistance increases. In the CV mode, the relative errors will decrease as the load resistance increases.

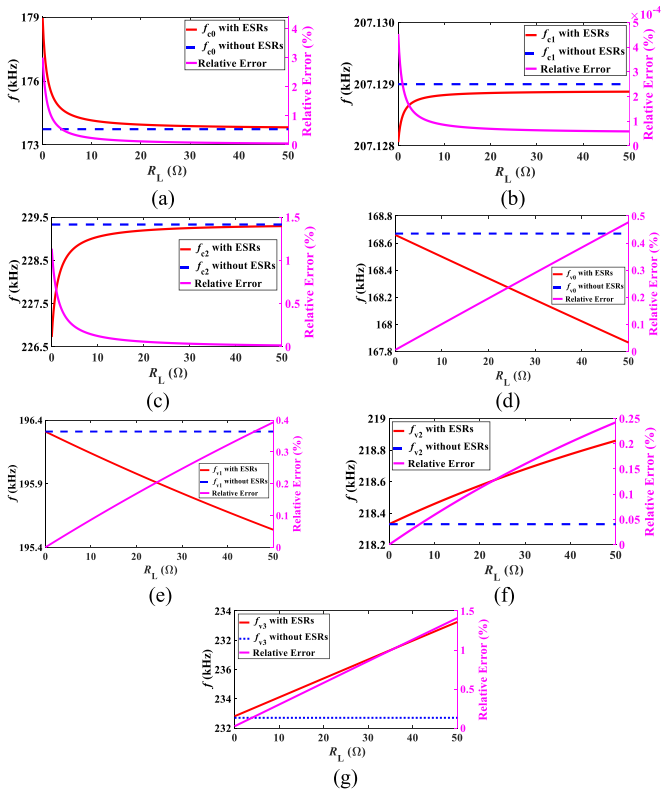

Fig. 11. Comparative curves of $f_{\rm init}$ determined by ideal and modified calculation equations for the domino WPT system with ESR = 0.3 Ω. (a) f_{c0}. (b) f_{c1}. (c) f_{c2} (d) f_{v0}. (e) f_{v1}. (f) f_{v2}. (g) f_{v3}.

The proposed double-layer PWPFC are designed based on simple logics and equations with low computation burden. The searching algorithms in both upper and lower layers are well-established digital optimization algorithms that can be easily implemented using inexpensive microcontroller units. Even so, the proposed control strategy can accurately regulate the outputs, while track the MEET for domino WPT systems with ESRs over a wide range of load conditions.

IV. Experimental Verifications

Experiments are conducted on a four-coil domino SS-compensated WPT system with the parameters given in Table III. The minimum transconductance $G_{c\min}$ and the minimum voltage gain $G_{v\min}$ are set to be 0.04 A/V and 0.5 V/V, respectively. The maximum deviations $\sigma_{c\max}$ and $\sigma_{v\max}$ are set to be 5%. The photograph of the experimental setup is shown in Fig. 12. The dc power supply is RIGOL DP832. The primary-side GaN E-HEMT full-bridge inverter is GS61004B-EVBCD. The domino coils, which are wound by 2 mm Litz wires with 12 turns, are

TABLE III
MAIN PARAMETERS OF THE SYSTEM IN EXPERIMENT

Parameters	Value	Parameters	Value	Parameters	Value
U_{dc}	10 V	L_3	49.5 μH	M_{23}	9.98 μH
L_1	49.7 μH	C_3	12.87 nF	M_{34}	9.83 μH
C_1	12.87 nF	R_3	0.31 Ω	M_{13}	3.63 μH
R_1	0.31 Ω	L_4	49.4 μH	M_{24}	3.83 μH
L_2	49.6 μH	C_4	12.81 nF	M_{14}	1.72 μH
C_2	12.86 nF	R_4	0.38 Ω	C_f	15.2 μF
R_2	0.3 Ω	M_{12}	9.97 μH	R_L	10–41.6 Ω

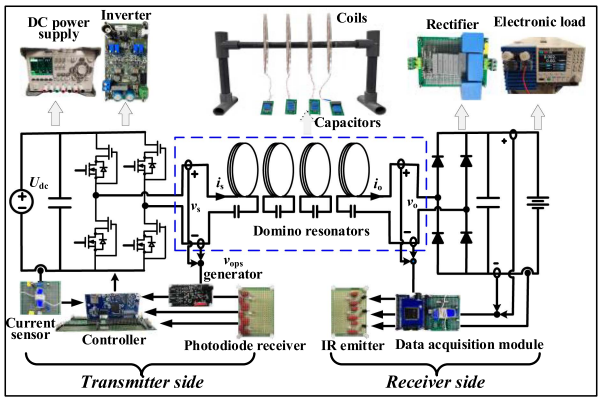

Fig. 12. Schematic diagram of the experimental setup.

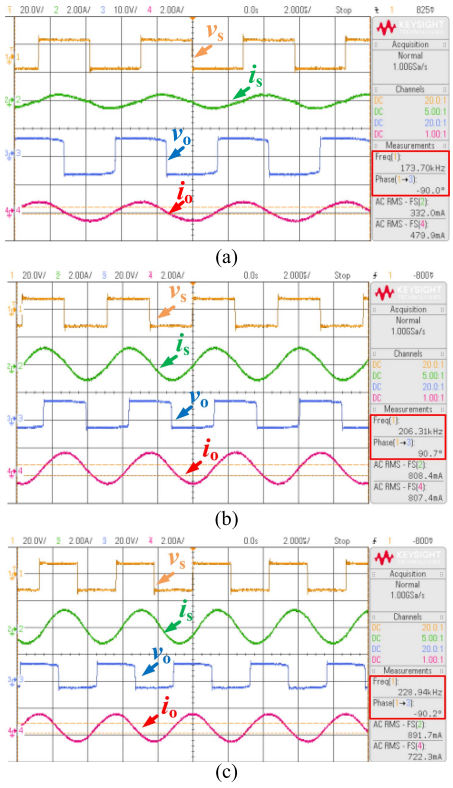

Fig. 13. Experimental waveforms of v_s, i_s, v_o, and i_o at the three QLI CC frequencies (i.e., (a) $f = f_{c0}$, (b) $f = f_{c1}$, and (c) $f = f_{c2}$).

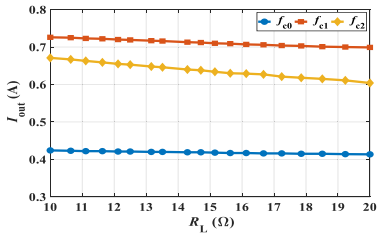

Fig. 14. I_{out} of the WPT system at the three QLI CC frequencies with different load conditions.

spiral. The dimension of the spiral coils is 23cm. The distance between the two neighboring spiral coils is fixed at 7 cm. The coils are compensated by series plastic film capacitors at the resonant frequency of 200 kHz. The battery load is emulated by the electronic load KIKUSUI PLZ405W. The diode bridge rectifier is implemented by four ISL9R860P2. The current sensors for measuring I_{dc} and I_{out} at both the transmitter and receiver sides are LEM 25-P. The voltage sensor for measuring U_{out} is made by a simple voltage divider with the resistors of 20 and 35 kΩ. The TMS320F28379D Experimenter Kit is adopted for the primary-side controller. The phase difference between v_s and v_o are calibrated by the high-speed dual-comes comparator TI TLV3502 and single two-input positive-AND gate TI SN74AHC1G0. The feedback signals (i.e., U_{out}, I_{out}, and phase of v_o) are transmitted wirelessly from the emitter VSLY3850 on the receiver side to the photodiode SFH213 on the transmitter side. The communication delay of the adopted infrared (IR) communication is negligible for the investigated system operating at kilohertz frequency levels [30].

A. QLI CC Outputs of the SS-Compensated WPT System

For the nominal load condition of CC mode $R_L = 10\ \Omega$, by nullifying the real part of (16.1), the initial operating frequencies of the WPT system for QLI CC outputs can be calculated based on (16.1) as $f_{c0} = 173.81$ kHz, $f_{c1} = 206.53$ kHz, and $f_{c2} = 229.26$ kHz. The waveforms of v_s, i_s, v_o, and i_o of the WPT system operating at the three QLI CC frequencies are presented in Fig. 13. The phase differences between v_s and v_o are 90° for all the three cases. The relative errors σ_c are calculated based on (11.1) as 2.35%, 3.85%, and 11.94%, respectively. Apparently, f_{c2} is forfeited since its σ_c is beyond the 5% limit. The output current of the system operating at the three QLI CC frequencies with different load conditions are plotted, as shown in Fig. 14. In accordance with the calculation results of the relative errors, f_{c0} has the minimum output current fluctuations from 0.424 to 0.4135 A over the load range from 10 to 20 Ω. The output current fluctuations of f_{c1} are ranging from 0.726 A to 0.699 A. f_{c2} has the biggest output deviations (about 10.3%). Subsequently, by employing the reference selection algorithm in Fig. 7, the overall efficiencies of the WPT system with the acceptable frequencies f_{c0} and f_{c1} are compared. The optimal frequency is determined by identifying the one that yields the highest efficiency. The overall efficiencies of the system operating at the three QLI CC frequencies with different load conditions are plotted as shown in Fig. 15. Obviously, the efficiencies of f_{c1} are higher than those of f_{c0} and f_{c2}. Hence, f_{c1} is selected as the optimal operating frequency for QLI CC outputs.

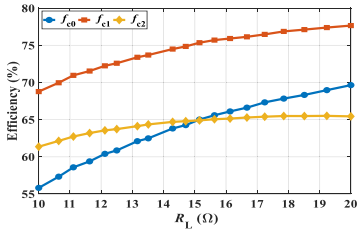

Fig. 15. Overall efficiencies of the WPT system at the three QLI CC frequencies with different load conditions.

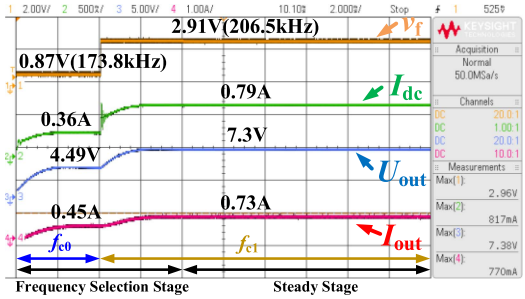

Fig. 16. Experimental waveforms of v_f, $I_{\rm dc}$, $U_{\rm out}$, and $I_{\rm out}$ during the frequency selection stage for QLI CC outputs and maximum efficiency operations.

To validate the effectiveness of the proposed control strategy to regulate the system operating at optimal frequencies, the transient waveforms of v_f, $I_{\rm dc}$, $U_{\rm out}$, and $I_{\rm out}$ of the WPT system with $R_L = 10\ \Omega$ during the initial frequency selection stage are presented, as shown in Fig. 16. Here, v_f is the digital-to-analogue output of the digital controller (i.e., $v_f = 0.0063 \times (\frac{f}{100} - 1600)$. It is directly measured by the voltage probe to indicate the operating frequency of the system. $v_f = 0.87$ V and $v_f = 2.91$ V indicate the switching frequencies of the primary-side inverter to be 173.8 and 206.5 kHz, respectively. Since σ_c of f_{c2} exceeds the upper limit, only the efficiencies of f_{c0} and f_{c1} are evaluated during the frequency selection stage. The overall system efficiencies with f_{c0} and f_{c1} are 56% and 67.5%, respectively. The selection period of each frequency is set to be 4 ms. Eventually, the system settles at f_{c1} for QLI CC outputs and maximum efficiency.

After the execution of the frequency selection algorithm in stage-I, the operating frequency of the system is subsequently controlled by the proposed tracking algorithm in Stage-II to lock at the optimal frequency. The steady-state waveforms of v_s, v_o, i_o, and $v_{\rm ops}$ are shown in Fig. 17. The duty ratio of the pulse signal $v_{\rm ops}$ being generated by the AND gate, i.e., $D_{\rm ops}$, is obtained using the enhanced capture (eCAP) function of the digital signal processor. The eCAP module can accurately capture the timing of significant external events and is frequently employed for measuring the period and duty cycle of pulse train signals. Here, $D_{\rm ops}$ is regulated at 0.245, exhibiting a negligible error of 2% as compared to the reference $D_{\rm ref} = 0.25$ for CC outputs (mainly caused by the frequency step restrictions of the digital controller). The operating frequency is locked at 206.06 kHz, which is close to the optimal $f_{c1} = 206.53$ kHz.

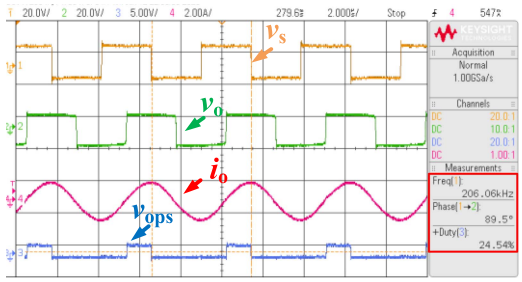

Fig. 17. Steady-state waveforms of v_s, v_o, i_o, and $v_{\rm ops}$ of the system controlled by the tracking algorithm for optimal frequency lock in the CC mode.

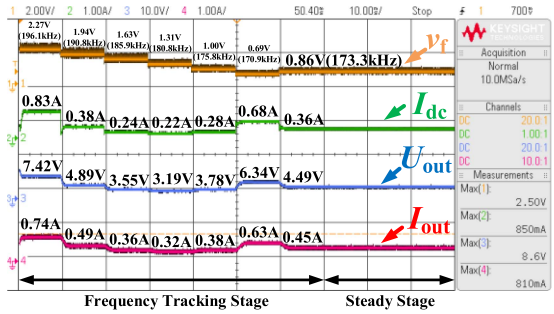

Fig. 18. Dynamic waveforms of v_f, $I_{\rm dc}$, $U_{\rm out}$, and $I_{\rm out}$ of the system with the manual set initial frequency at $f_{c0} = 173.3$ kHz in the CC mode.

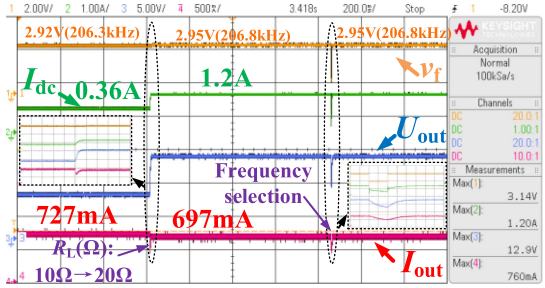

Fig. 19. Dynamic waveforms of v_f, $I_{\rm dc}$, $U_{\rm out}$, and $I_{\rm out}$ of the system with R_L charging from 10 to 20 Ω in the CC mode.

To verify the importance of the proposed initial frequency determination in the tracking algorithm, the initial frequency $f_{\rm init}$ is manually configured to be 196.1 kHz (the corresponding $v_f = 2.27$ V) and the frequency change step Δf is set to be -5 kHz (the corresponding $\Delta v_f = -0.0315$ V). The dynamic waveforms of v_f, $I_{\rm dc}$, $U_{\rm out}$, and $I_{\rm out}$ are presented in Fig. 18. The operating frequency is eventually converged at $f_{c0} = 173.3$ kHz and the overall system efficiency is only 56%.

To showcase the QLI CC output characteristics of the WPT system with the proposed control strategy, R_L is changed from 10 Ω to 20 Ω. The dynamic waveforms of v_f, $I_{\rm dc}$, $U_{\rm out}$, and $I_{\rm out}$ are presented, as shown in Fig. 19. The operating frequency is consistently optimized at f_{c1}. For the nominal $R_L = 10\ \Omega$, $I_{\rm out}$ is 0.728 A. For $R_L = 20\ \Omega$, $I_{\rm out}$ is 0.698 A. The relative error is only 4.12%. Thus, QLI CC outputs of the system are implemented using the proposed control strategy.

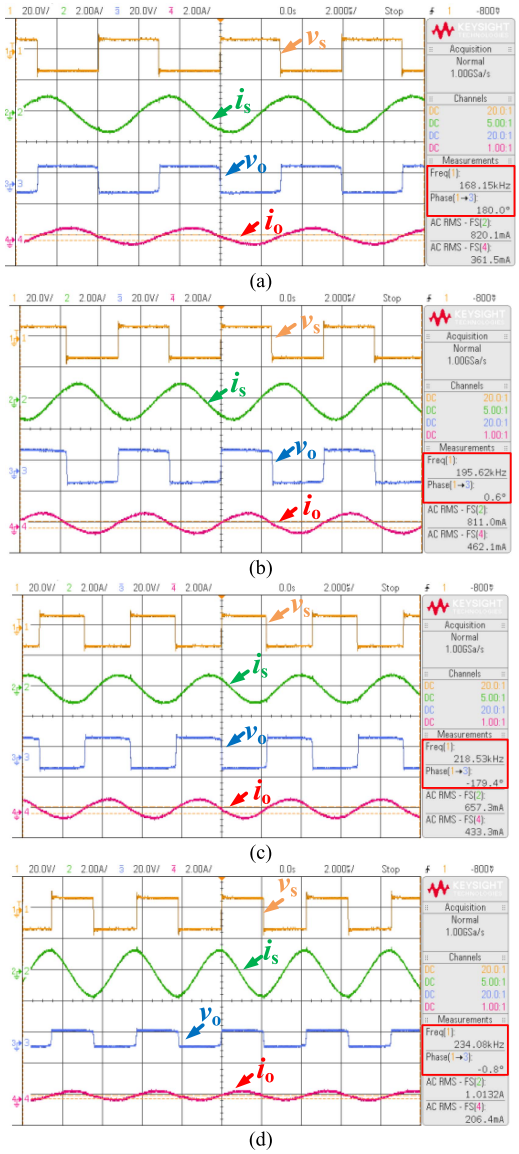

Fig. 20. Experimental waveforms of v_s, i_s, v_o, and i_o at the four QLI CV frequencies (i.e., (a) $f = f_{v0}$, (b) $f = f_{v1}$, (c) $f = f_{v2}$, and (d) $f = f_{v3}$).

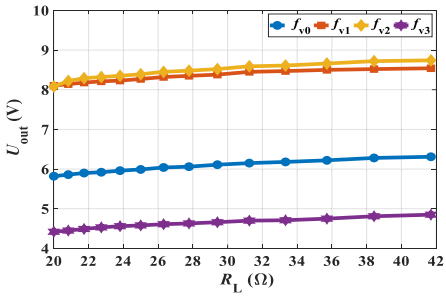

Fig. 21. $U_{\rm out}$ of the WPT system at the four QLI CV frequencies with different load conditions.

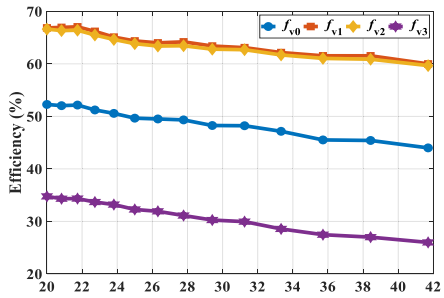

Fig. 22. Overall efficiencies of the WPT system at the four QLI CV frequencies with different load conditions.

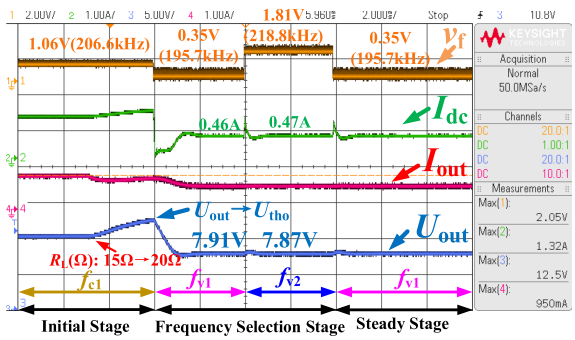

Fig. 23. Experimental waveforms of v_f, $I_{\rm dc}$, $I_{\rm out}$, and $U_{\rm out}$ during the frequency selection stage for QIL CV outputs and maximum efficiency operations.

B. QLI CV Outputs of the SS-Compensated WPT System

Similar to the procedures of deriving multiple QLI CC frequencies, four QLI CV frequencies (i.e., $f_{v0} = 168.16$ kHz, $f_{v1} = 195.74$ kHz, $f_{v2} = 218.96$ kHz, and $f_{v3} = 233.97$ kHz) can be calculated by nullifying the imaginary part of (16.2) for the nominal load condition of CV mode $R_L = 20\ \Omega$. The corresponding voltage gains of the system can be derived as -0.86, 0.96, -0.94, and 0.56, respectively. According to the signs of the voltage gains, $D_{\rm ref}$ of the four frequencies are 0, 0.5, 0, 0.5. Thus, the phase difference between v_s and v_o are 180°, 0°, 180°, and 0°. The waveforms of v_s, i_s, v_o, and i_o are shown in Fig. 20. v_o is in phase with v_o at f_{v1} and f_{v3}, and in reverse phase with v_o at f_{v0} and f_{v2}. Apparently, the practical results are in good agreement with the theoretical derivations.

Based on (11.2), σ_v of the four frequencies at the nominal load condition can be calculated as 7.63%, 4.16%, 4.79%, and 8.32%, respectively. Since σ_v of f_{v0} and f_{v3} are beyond the 5% limit, they are excluded for further efficiency comparisons. Experiments are also conducted on the WPT system with different load conditions from the nominal 20 to 41.6 Ω. The corresponding $U_{\rm out}$ and overall system efficiencies are exhibited, as shown in Figs. 21 and 22. It can be observed that the efficiencies of $f_{\rm v1}$ are higher those of other frequencies. Therefore, $f_{\rm v1}$ should be selected as the optimal frequency.

The transient waveforms of v_f, $I_{\rm dc}$, $U_{\rm out}$, and $I_{\rm out}$ of the WPT system with $R_L = 20\ \Omega$ during the initial frequency selection stage are shown in Fig. 23. In the CV mode, the relationship between v_f and f is $v_f = 0.0063 \times (\frac{f}{100} - 1900)$. The threshold voltage $U_{\rm tho}$ is 12.5 V. Since f_{v0} and f_{v3} are exempted for efficiency comparisons, only the efficiencies of the system operating at f_{v1} and $f_{\rm v2}$ are evaluated. The selection period is set to be 8ms for the two frequencies. Finally, the system settles at f_{v1} since its efficiency 68.01% is higher than 65.98% of f_{v2}.

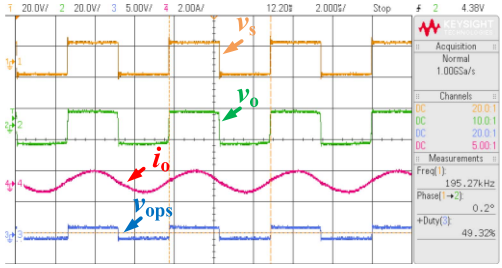

Fig. 24. Steady-state waveforms of v_s, v_o, i_o, and $v_{\rm ops}$ of the system controlled by the tracking algorithm for optimal frequency lock in the CV mode.

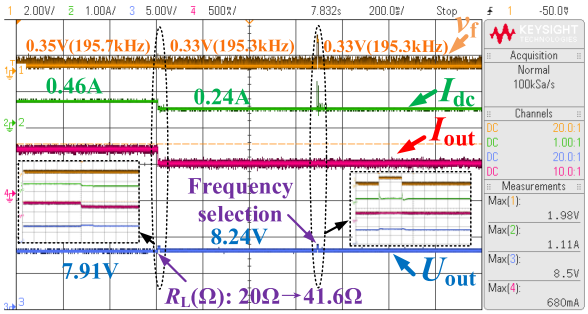

Fig. 25. Dynamic waveforms of v_f, $I_{\rm dc}$, $I_{\rm out}$, and $U_{\rm out}$ of the system with R_L charging from 20 to 41.6 Ω in the CV mode.

Then, the propose tracking algorithm in stage-II is adopted to regulate the system at the optimal frequency. The steady-state waveforms of v_s, v_o, i_o, and $v_{\rm ops}$ are shown in Fig. 24. $D_{\rm ops}$ is controlled at 0.493, with a negligible error as compared to the reference $D_{\rm ref} = 0.5$ for CV outputs. The operating frequency 195.27 kHz is close to the calculated $f_{\rm v1} = 195.74$ kHz.

The dynamic waveforms of v_f, $I_{\rm dc}$, $I_{\rm out}$, and $U_{\rm out}$ of the WPT system with load resistance varying from $R_L = 20\ \Omega$ to from $R_L = 41.6\ \Omega$ are shown in Fig. 25. The operating frequency is consistently optimized at $f_{\rm v1}$. For the nominal $R_L = 20\ \Omega$, $U_{\rm out}$ is 7.91 V. For $R_L = 41.6\ \Omega$, $U_{\rm out}$ is 8.24 V. The relative error is only 4.17%. QLI CV outputs of the system can be achieved.

C. Performance of WPT Systems With Other Compensations

Experiments are also carried out on WPT systems with other compensation networks. The waveforms of v_f, $I_{\rm dc}$, $U_{\rm out}$, and $I_{\rm out}$ of the *LCC-LCC*-compensated WPT system with step load changes in both CC and CV modes are shown in Fig. 26. The relationship between v_f and f is $v_f = 0.0033 \times (\frac{f}{100} - 1600)$. The operating frequencies are controlled at $f_{c0} = 174.1$ kHz and $f_{v0} = 183.8$ kHz for ensuring the relative errors of the outputs (i.e., 1.27% and 4.95%) being less than the upper constraints of QLI CC and CV outputs, and the overall system efficiencies are maximized among all those QLI frequencies. The efficiencies of WPT systems with other compensation schemes operating at QLI frequencies are given in Table IV. The optimal frequencies for maximum efficiencies are highlighted. The output deviations of the optimal frequencies are verified to be well-regulated within the constraints, which indicate that the QLI CC and CV outputs can be achieved.

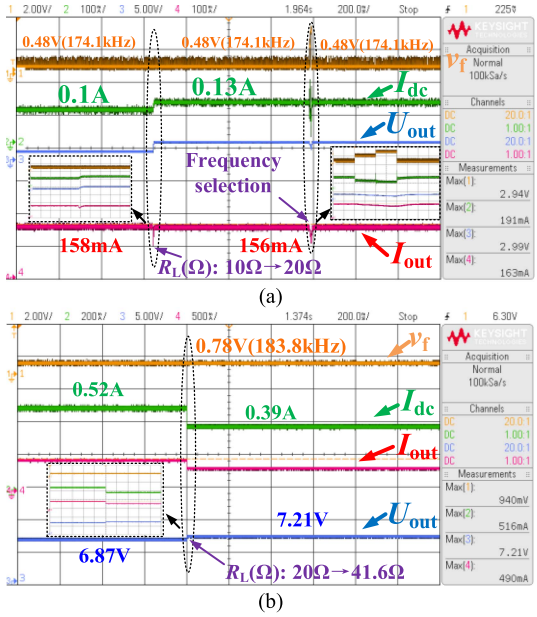

Fig. 26. Waveforms of v_f, $I_{\rm dc}$, $U_{\rm out}$, and $I_{\rm out}$ of the LCC-LCC-compensated WPT system with step load changes in the (a) CC mode and (b) CV mode.

TABLE IV
OVERALL EFFICIENCIES OF WPT SYSTEMS WITH VARIOUS COMPENSATION SCHEMES

Comp. Type	Overall Efficiencies (%)															
	10 Ω (CC) nominal				20 Ω (CC)				20 Ω (CV) nominal				41.6 Ω (CV)			
	f_{c0}	f_{c1}	f_{c2}	f_{c3}	f_{c0}	f_{c1}	f_{c2}	f_{c3}	f_{v0}	f_{v1}	f_{v2}	f_{v3}	f_{v0}	f_{v1}	f_{v2}	f_{v3}
LCC-LCC	**24**	23	17	–	**34**	18	15	–	**45**	–	–	–	**32**	–	–	–
LCC-S	–	42	**48**	1	–	56	**58**	1	**50**	37	16	–	**40**	28	11	–
SS	55	**69**	–	–	68	**78**	–	–	–	**67**	66	–	–	**60**	59	–

V. CONCLUSION

In this article, a double-layer pulse-width PWPFC is proposed for domino WPT systems in achieving QLI CC and CV outputs, while simultaneously operating with MEET. The proposed double-layer PWPFC is applied for the primary-side inverters of domino WPT systems with full considerations of ESRs of the resonators. Experimental results validate the effectiveness of the proposed control in regulating four-coil WPT systems with any compensation networks of the transmitters and receivers. Maximum efficiencies and minimum output deviations are implemented under various operating conditions.

APPENDIX

A. Verifications of Unity Voltage Gains in the CV Mode

For the ideal four-coil domino WPT system with perfect compensation and neglected ESRs, (3.1) can be simplified as

$$\begin{bmatrix} v_s \\ 0 \\ 0 \\ 0 \end{bmatrix} = \begin{bmatrix} j\omega L' & j\omega M_1 & j\omega M_2 & j\omega M_3 \\ j\omega M_1 & j\omega L' & j\omega M_1 & j\omega M_2 \\ j\omega M_2 & j\omega M_1 & j\omega L' & j\omega M_1 \\ j\omega M_3 & j\omega M_2 & j\omega M_1 & j\omega L' + R_{\rm L} \end{bmatrix} \begin{bmatrix} i_1 \\ i_2 \\ i_3 \\ i_4 \end{bmatrix} \quad \text{(A1)}$$

where $M_1 = M_{12} = M_{23} = M_{34}, M_2 = M_{13} = M_{24}, M_3 = M_{14}$, $L' = L_i\ (1 - \frac{\omega_0^2}{\omega^2})$, and $\omega_0 = \frac{1}{\sqrt{L_1 C_1}} = \frac{1}{\sqrt{L_2 C_2}} = \frac{1}{\sqrt{L_3 C_3}} = \frac{1}{\sqrt{L_4 C_4}}$. Based on (A1), i_1, i_2, and i_3 can be derived as

$$i_1 = -\frac{(L' i_2 + M_1 i_3 + M_2 i_4)}{M_1} \tag{A2}$$

$$i_2 = \frac{M_1 (L' - M_2) i_3 + (M_1^2 - M_2^2) i_4}{L' M_2 - M_1^2} \tag{A3}$$

$$i_3 = \frac{\omega\left[M_2\left(M_1^2 + M_1 M_3 + L'^2 - M_2^2\right) - M_1 L'(M_1 + M_3)\right] + j(M_1^2 - M_2 L') R_L}{\omega(M_1^3 + M_1 M_2^2 + M_3 L'^2 - 2M_1 M_2 L' - M_3 M_1^2)} i_4. \tag{A4}$$

By substituting (A2), (A3), and (A4) into (A1), the relationships between v_s and v_o can be derived as

$$v_s = \frac{B + \frac{A}{R_L} j}{M_1^3 + M_1 M_2^2 + M_3 L'^2 - M_3 M_1^2 - 2M_1 M_2 L'} v_o \tag{A5}$$

where

$$A = -\omega\left[(M_1 - M_2)^2 + (M_1 + M_3) L' - M_1 M_3 - L'^2\right] \times \left[(M_1 + M_2)^2 - (M_1 + M_3) L' - M_1 M_3 - L'^2\right] \tag{A6}$$

and

$$B = (M_2 - L')\left(L'^2 + M_2 L' - 2M_1^2\right). \tag{A7}$$

According to (A5), load-independent CV outputs can be realized by nullifying the coefficient A. The corresponding voltage gain is

$$G_v = \frac{v_o}{v_s} = \frac{M_1^3 + M_1 M_2^2 + M_3 L'^2 - M_3 M_1^2 - 2M_1 M_2 L'}{B}. \tag{A8}$$

If $(M_1 - M_2)^2 + (M_1 + M_3)L' - M_1 M_3 - L'^2 = 0$, the relationship between ω and ω_o can be derived as

$$\left[(M_1 - M_2)^2 + (M_1 + M_3 - L_1) L_1 - M_1 M_3\right] \omega^4 + \omega_0^2 L_1 (2L_1 - M_1 - M_3) \omega^2 - L_1^2 \omega_0^4 = 0 \tag{A9}$$

and

$$M_3 = \frac{(M_1 - M_2)^2 + M_1 L' - L'^2}{M_1 - L'}. \tag{A10}$$

By substituting (A10) into (A8)

$$G_v = \frac{M_1\left(M_1^2 + M_2^2 - 2M_2 L'\right) - \left[(M_1 - M_2)^2 + M_1 L' - L'^2\right](L' + M_1)}{B} = -1. \tag{A11}$$

If $(M_1 + M_2)^2 - (M_1 + M_3)L' - M_1 M_3 - L'^2 = 0$, the relationship between ω and ω_o can be derived as

$$\left[(M_1 + M_2)^2 - L_1 (M_1 + M_3 + L_1) - M_1 M_3\right] \omega^4 + \omega_0^2 L_1 (2L_1 + M_1 + M_3) \omega^2 - L_1^2 \omega_0^4 = 0 \tag{A12}$$

TABLE V
PROPERTIES OF EACH COMPONENT OF THE TWO FUNCTIONS

Component	Property	Component	Property
$a_{T(R)11}$	$\Re$	$a_{T(R)12}$	$\Im$ or 0
$a_{T(R)21}$	$\Im$ or 0	$a_{T(R)22}$	$\Re$
G_1	$\Im$	G_2	$\Re$
F_1	$\Im$	F_2	$\Re$
α	$\Im$	β	$\Im$

and

$$M_3 = \frac{(M_1 + M_2)^2 - M_1 L' - L'^2}{M_1 + L'}. \tag{A13}$$

By substituting (A13) into (A8)

$$G_v = \frac{M_1\left(M_1^2 + M_2^2 - 2M_2 L'\right) + \left[(M_1 + M_2)^2 - M_1 L' - L'^2\right](L' - M_1)}{B} = 1. \tag{A14}$$

It can be seen from (A11) and (A14) that the voltage gains (i.e., $|G_v|$) are unity and they are independent from the system parameters.

B. *Verifications of* $D_{ref} = 0.25$ *in the CC Mode and* $D_{ref} = 0$ *or 0.5 in the CV Mode*

The transfer ratio of v_s over v_o can be derived based on (8.2) as

$$\frac{v_s}{v_o} = \frac{f_v(\omega)}{R_L} + f_c(\omega). \tag{A15}$$

The real ($\Re$) and imaginary ($\Im$) properties of the components of $f_c(\omega)$ and $f_v(\omega)$ are given in Table V. Based on (8.3) and (8.4), $f_v(\omega)$ is found to be pure imaginary ($\Im$) if $f_c(\omega)$ is zero. On the other hand, $f_c(\omega)$ is pure real ($\Re$) if $f_v(\omega)$ is zero. Thus, according to (A15), v_o leads or lags v_s with 90° in the CC mode. To achieve that, the duty ratio reference D_{ref} of driving signal (the square wave pulse generated by the AND logic gate in stage-II) must be 0.25. In the CV mode, v_o is in phase or reverse phase with v_s. According to (A15), D_{ref} is either 0 or 0.5. By substituting f_{ref} into (A15), the sign of the voltage gain G_v can be obtained. If G_v is positive, D_{ref} is 0.5. If G_v is negative, D_{ref} is 0.

REFERENCES

[1] S. Y. R. Hui, W. Zhong, and C. K. Lee, "A critical review of recent progress in mid-range wireless power transfer," *IEEE Trans. Power Electron.*, vol. 29, no. 9, pp. 4500–4511, Sep. 2014.

[2] S. Moon, B.-C. Kim, S.-Y. Cho, C.-H. Ahn, and G.-W. Moon, "Analysis and design of a wireless power transfer system with an intermediate coil for high efficiency," *IEEE Trans. Ind. Electron.*, vol. 61, no. 11, pp. 5861–5870, Nov. 2014.

[3] K. Lee and S. H. Chae, "Power transfer efficiency analysis of intermediate-resonator for wireless power transfer," *IEEE Trans. Power Electron.*, vol. 33, no. 3, pp. 2484–2493, Mar. 2018.

[4] Y. Li, Q. Xu, T. Lin, J. Hu, Z. He, and R. Mai, "Analysis and design of load-independent output current or output voltage of a three-coil wireless power transfer system," *IEEE Trans. Transp. Electrific.*, vol. 4, no. 2, pp. 364–375, Jun. 2018.

[5] Y. Yang, H. W. R. Liang, S. C. Tan, and S. Y. R. Hui, "Design of a wireless power modulator for wireless power transfer systems," in *Proc. IEEE 12th Energy Convers. Congr. Expo.-Asia*, 2021, pp. 816–820.

[6] C. K. Lee, W. X. Zhong, and S. Y. R. Hui, "Effects of magnetic coupling of nonadjacent resonators on wireless power domino-resonator systems," *IEEE Trans. Power Electron.*, vol. 27, no. 4, pp. 1905–1916, Apr. 2012.

[7] W. Zhong, C. K. Lee, and S. Y. R. Hui, "General analysis on the use of Tesla's resonators in domino forms for wireless power transfer," *IEEE Trans. Ind. Electron.*, vol. 60, no. 1, pp. 261–270, Jan. 2013.
[8] W. X. Zhong, C. K. Lee, and S. Y. Hui, "Wireless power domino resonator systems with non-coaxial axes and circular structures," *IEEE Trans. Power Electron.*, vol. 27, no. 11, pp. 4750–4762, Nov. 2012.
[9] Z. Dong, S. Liu, X. Li, Z. Xu, and L. Yang, "A novel long-distance wireless power transfer system with constant current output based on domino-resonator," *IEEE J. Emerg. Sel. Topics Power Electron.*, vol. 9, no. 2, pp. 2343–2355, Apr. 2021.
[10] S. Liu, Y. Feng, H. Chen, J. Wu, and X. He, "Multi-coil constant voltage output analysis based on state deconstruction for wireless power transfer system," in *Proc. IEEE Energy Convers. Congr. Expo.*, 2021, pp. 5704–5708.
[11] X. Hou, Y. Su, Z. Zuo, X. Dai, and Y. Fei, "A novel analysis method based on quadratic eigenvalue problem for multirelay magnetic coupling wireless power transfer," *IEEE Trans. Power Electron.*, vol. 36, no. 9, pp. 9907–9917, Sep. 2021.
[12] X. Hou, H. Hu, Y. Su, Z. Liu, Z. Deng, and R. Deng, "A multirelay wireless power transfer system with double-sided LCC compensation network for online monitoring equipment," *IEEE J. Emerg. Sel. Topics Power Electron.*, vol. 11, no. 1, pp. 1262–1271, Feb. 2023.
[13] J. Wang et al., "Communication-free long-distance wireless charging system for battery load with adaptive switching of constant voltage and constant current," *IEEE Trans. Transp. Electrific.*, early access, Jul. 14, 2023, doi: 10.1109/TTE.2023.3294513.
[14] C. Cheng, Z. Zhou, W. Li, C. Zhu, Z. Deng, and C. C. Mi, "A multi-load wireless power transfer system with series-parallel-series compensation," *IEEE Trans. Power Electron.*, vol. 34, no. 8, pp. 7126–7130, Aug. 2019.
[15] C. Cheng et al., "A load-independent LCC-compensated wireless power transfer system for multiple loads with a compact coupler design," *IEEE Trans. Ind. Electron.*, vol. 67, no. 6, pp. 4507–4515, Jun. 2020.
[16] Z. Dongye et al., "An S-CLC compensated load-independent inductive power relay system with constant voltage outputs," *IEEE Trans. Power Electron.*, vol. 36, no. 5, pp. 5157–5168, May 2021.
[17] C. Cheng, Z. Zhou, W. Li, Z. Deng, and C. C. Mi, "A power relay system with multiple loads using asymmetrical coil design," *IEEE Trans. Ind. Electron.*, vol. 68, no. 2, pp. 1188–1196, Feb. 2021.
[18] Z. Zhou, Z. Deng, C. Cheng, W. Li, F. Li, and C. Mi, "A wireless power transfer system with multiple constant current and constant voltage outputs," in *Proc. IEEE Energy Convers. Congr. Expo.*, 2019, pp. 4976–4981.
[19] Y. Wang, Z. Dongye, H. Zhang, C. Zhu, and F. Lu, "A domino-type load-independent inductive power transfer system with hybrid constant-current and constant-voltage outputs," *IEEE Trans. Power Electron.*, vol. 36, no. 8, pp. 8824–8834, Aug. 2021.
[20] C. Zhang, D. Lin, N. Tang, and S. Y. R. Hui, "A novel electric insulation string structure with high-voltage insulation and wireless power transfer capabilities," *IEEE Trans. Power Electron.*, vol. 33, no. 1, pp. 87–96, Jan. 2018.
[21] J. Qu, L. He, N. Tang, and C. K. Lee, "Wireless power transfer using domino-resonator for 110-kV power grid online monitoring equipment," *IEEE Trans. Power Electron.*, vol. 35, no. 11, pp. 11380–11390, Nov. 2020.
[22] Y. Fang, J. Qu, B. M. H. Pong, C. K. Lee, and R. S. Y. Hui, "Quasi-static modeling and optimization of two-layer PCB resonators in wireless power transfer systems for 110-kV power grid online monitoring equipment," *IEEE Trans. Ind. Electron.*, vol. 69, no. 2, pp. 1400–1410, Feb. 2022.
[23] Y. Guan, R. Sun, Y. Xiao, Y. Wang, and D. Xu, "Optimization and design of multi-relay wireless power transfer system in insulator with metal flanges," in *Proc. 48th Annu. Conf. IEEE Ind. Electron. Soc.*, 2022, pp. 1–6.
[24] Z. Yan et al., "A monitoring equipment charging system for HVTL based on domino-resonator WPT with constant current or constant voltage output," *IEEE Trans. Power Electron.*, vol. 37, no. 3, pp. 3668–3680, Mar. 2022.
[25] P. Gu et al., "A 2.5m long-range IPT system based on domino cylindrical solenoid coupler compensated respectively in layers," *IEEE Trans. Ind. Electron.*, vol. 70, no. 2, pp. 1409–1420, Feb. 2023.
[26] P. Gu et al., "A three-stage-five-coil IPT system based on cylindrical solenoid coupler applied to state detection equipment of HV device," *IEEE Trans. Power Electron.*, vol. 37, no. 2, pp. 2382–2393, Feb. 2022.
[27] C. Cai et al., "Resonant wireless charging system design for 110-kV high-voltage transmission line monitoring equipment," *IEEE Trans. Ind. Electron.*, vol. 66, no. 5, pp. 4118–4129, May 2019.
[28] X. Ren et al., "Characterization and control of self-oscillating contactless resonant converter with fixed voltage gain," in *Proc. 7th Int. Power Electron. Motion Control Conf.*, 2012, pp. 1822–1827.
[29] Y. Liu, J. Chen, Y. Li, and Z. He, "A new modeling method for multiple-relay wireless power transfer system considering cross-coupling," *IEEE Trans. Ind. Electron.*, vol. 71, no. 2, pp. 1456–1467, Feb. 2024.
[30] E. Gati, G. Kampitsis, and S. Manias, "Variable frequency controller for inductive power transfer in dynamic conditions," *IEEE Trans. Power Electron.*, vol. 32, no. 2, pp. 1684–1696, Feb. 2017.

Kaiyuan Wang (Student Member, IEEE) received the B.Eng. degree in electrical engineering from Northeast Electric Power University in 2020, and the M.Sc. degree in electrical engineering from The University of Hong Kong, Hong Kong, in 2021 and the M.Phil. degree in electrical engineering from Hong Kong Polytechnic University, Hong Kong in 2023. He is currently working toward the Ph.D. degree in electrical engineering with Nanyang Technological University, Singapore.

His research interests include wireless power transfer and power electronics.

Mr. Wang is a recipient of the 12th APSCOM2022 best paper award.

Junming Zeng (Student Member, IEEE) received the B.Eng. degree in electrical engineering and automation from the School of Automation, Guangdong University of Technology, Guangzhou, China, in 2020 and the M.Sc. degree in power engineering in 2021 from the Nanyang Technological University, Singapore, where he is currently working toward the Ph.D. degree in electrical and electronic engineering.

His current research interests include wireless power transfer and power electronics.

Yun Yang (Senior Member, IEEE) received the B.Sc. degree from Wuhan University, Wuhan, China, in 2012 and the Ph.D. degree in from the University of Hong Kong, Hong Kong, in 2017, both in electrical engineering.

He was a Research Assistant Professor with the Department of Electrical Engineering, The Hong Kong Polytechnic University. He is currently an Assistant Professor with the School of Electrical and Electronic Engineering, Nanyang Technological University, Singapore. His research interests include wireless power transfer, renewable energy technologies, electric vehicles, power electronics, and advanced control.

Shu Yuen Ron Hui (Fellow, IEEE) received the B.Sc. (Eng.; Hons.) degree in electrical and electronic engineering from the University of Birmingham, Birmingham, U.K., in 1984, and the D.I.C. and Ph.D. degrees in electrical engineering from Imperial College London, London, U.K., in 1987.

He is currently a Philip Wong Wilson Wong Professor with the University of Hong Kong, Hong Kong, and a Chair Professorship of power electronics with Imperial College London, London, U.K. He was the MediaTek Endowed Professorship with Nanyang Technological University. He has authored or coauthored more than 500 research papers, including 300 refereed journal publications. More than 120 of his patents have been adopted by industry worldwide. His inventions on wireless charging platform technology underpin key dimensions of Qi, the world's first wireless power standard, with freedom of positioning and localized charging features for wireless charging of consumer electronics. He has also developed the photoelectrothermal theory for LED systems and electric spring technology for smart grid. His research interests include power electronics, wireless power, sustainable lighting, and smart grid.

Dr. Hui was the recipient of the IEEE Rudolf Chope R&D Award and the IET Achievement Medal (The Crompton Medal) in 2010, and IEEE William E. Newell Power Electronics Award in 2015. He is a Fellow of the Australian Academy of Technological Sciences and Engineering, US National Academy of Inventors, and Royal Academy of Engineering, U.K.